

Tuning the Electrocatalytic Oxygen Reduction Reaction Activity and Stability of Shape-Controlled Pt–Ni Nanoparticles by Thermal Annealing – Elucidating the Surface Atomic Structural and Compositional Changes

Vera Beermann,[†] Martin Gocyla,[‡] Stefanie Köhl,[†] Elliot Padgett,[§] Henrike Schmieles,[†] Mikaela Goerlin,[†] Nina Erini,[†] Meital Shviro,[‡] Marc Heggen,[‡] Rafal E. Dunin-Borkowski,[‡] David A. Muller,^{§,⊥} and Peter Strasser^{*,†,⊥}

[†]Electrochemical Energy, Catalysis and Material Science Laboratory, Department of Chemistry, Technical University Berlin, 10623 Berlin, Germany

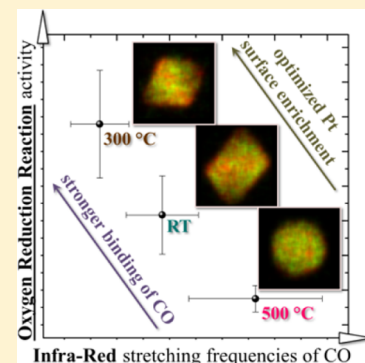
[‡]Ernst-Ruska Centre for Microscopy and Spectroscopy with Electrons and Peter Grünberg Institute, Forschungszentrum Jülich GmbH, 52425 Jülich, Germany

[§]School of Applied and Engineering Physics, Cornell University, Ithaca, New York 14850, United States

[⊥]Kavli Institute at Cornell for Nanoscale Science, Cornell University, Ithaca, New York 14850, United States

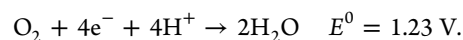
Supporting Information

ABSTRACT: Shape-controlled octahedral Pt–Ni alloy nanoparticles exhibit remarkably high activities for the electroreduction of molecular oxygen (oxygen reduction reaction, ORR), which makes them fuel-cell cathode catalysts with exceptional potential. To unfold their full and optimized catalytic activity and stability, however, the nano-octahedra require post-synthesis thermal treatments, which alter the surface atomic structure and composition of the crystal facets. Here, we address and strive to elucidate the underlying surface chemical processes using a combination of *ex situ* analytical techniques with *in situ* transmission electron microscopy (TEM), *in situ* X-ray diffraction (XRD), and *in situ* electrochemical Fourier transformed infrared (FTIR) experiments. We present a robust fundamental correlation between annealing temperature and catalytic activity, where a ~25 times higher ORR activity than for commercial Pt/C (2.7 A mg_{Pt}⁻¹ at 0.9 V_{RHE}) was reproducibly observed upon annealing at 300 °C. The electrochemical stability, however, peaked out at the most severe heat treatments at 500 °C. Aberration-corrected scanning transmission electron microscopy and energy-dispersive X-ray spectroscopy (EDX) in combination with *in situ* electrochemical CO stripping/FTIR data revealed subtle, but important, differences in the formation and chemical nature of Pt-rich and Ni-rich surface domains in the octahedral (111) facets. Estimating trends in surface chemisorption energies from *in situ* electrochemical CO/FTIR investigations suggested that balanced annealing generates an optimal degree of Pt surface enrichment, while the others exhibited mostly Ni-rich facets. The insights from our study are quite generally valid and aid in developing suitable post-synthesis thermal treatments for other alloy nanocatalysts as well.



INTRODUCTION

Due to the increasing demand for renewable and clean energy sources, research on electrolyzers, fuel cells, and other renewable energy technologies experienced a strong upturn in the past years. Over recent years, innovative, ever better performing Pt catalyst systems were developed for the overall efficiency-limiting oxygen reduction reaction (ORR) at the cathode of fuel cells, according to¹



For polymer electrolyte membrane fuel cell (PEMFC) cathodes, pure platinum nanoparticles are no longer state-of-the-art materials for the ORR, as they do not provide sufficient catalytic performance per cost at practical loadings. Recently

highlighted technical roadmaps toward reducing the noble metal cost of fuel cell catalysts have involved the transition from pure Pt catalysts to Pt alloys. It has been successfully shown that alloying Pt with 3d metals like Fe, Co, Ni, and Cu leads to improved activities, reduces the amount of Pt needed for desired fuel cell performance, and reduces the costs.^{2–9} Subsequently, an additional step change in cathode catalyst mass activity is envisaged to be provided by Pt alloy nanoparticles exhibiting specific surface orientations. By comparing well-defined single-crystal surfaces of Pt and Pt₃Ni in (111), (110), and (100) orientations, Stamenkovic et al. showed that Pt₃Ni (111) exhibits exceptional ORR activity in

Received: July 1, 2017

Published: October 11, 2017

acidic media.¹⁰ Certain nanoparticle shapes imply the preferred exposure of particular surface terminations, such as cubes (100 surfaces) or octahedra (111 surfaces) in cubic symmetries. Combining the benefits of alloying Pt and favorable shapes has resulted in record-breaking activities reported in recent years.^{11–16} In particular, octahedrally shaped Pt–Ni nanoalloys represent an especially active shape-controlled catalyst. Zhang et al. reported a wet-chemical synthesis of shape-controlled Pt₃Ni nanopolyhedra and confirmed the results of Stamenkovic et al. for nanoparticles supported on high surface area carbon.¹⁷ Cui et al. subsequently reported a DMF-based, surfactant-free synthesis of Pt–Ni octahedral nanoparticles and described the influence of the Pt–Ni surface composition on the ORR activity.^{18,19} Using a wet-chemical synthesis route including long-chain surfactants, Choi et al. were able to control size and composition of the octahedral Pt–Ni particles, resulting in high ORR activities.^{13,20} All these syntheses included a wide variety of distinct post-synthesis surface cleaning procedures, which turned out to be necessary as capping agents otherwise may have blocked ORR sites on the catalyst surface. Such post-synthesis treatments can involve complex multi-step washing, drying, and annealing protocols, which were often iteratively and empirically developed and the effect of which on the particle surface has therefore remained poorly understood. This is because post-synthesis treatments may combine surfactant cleaning with concomitant intended or unintended modifications in the surface structure and composition, which may or may not be conducive for the actual interfacial catalysis. Treatments with acid and alkaline solvents have also been described to successfully clean, modify, and tune particle surfaces and surface compositions,^{13,20–23} as well as a variety of thermal annealing procedures.^{24–26} A systematic analysis of the atomic-scale structural and compositional changes in the surface of shape-controlled PtNi alloy nanoparticles during post-synthesis treatment is missing. This contribution set out to change that.

To get molecular insight into how post-synthesis treatments affect the catalytic performance of octahedral PtNi nanocatalysts and help unfold unprecedented Pt mass-based activities for the ORR, we investigate here the correlation of thermal annealing and their surface structure, composition, and ORR activity and stability. What set this study apart from previous such studies is our focus on shape-controlled PtNi nanoparticles and their unprecedented high catalytic activity, and the combined use of a variety of *ex situ* and *in situ* techniques that allow conclusions as to the composition of the topmost layers of the octahedra.

First, we present studies on the particle behavior in terms of shape, distribution on the carbon support, and alloy conditions during heat treatment both *ex situ* and *in situ* by utilizing X-ray diffraction (XRD) and transmission electron microscopy (TEM). Second, we present electrochemical characterization of the Pt–Ni nanoparticles tested for the ORR, paying attention not only to their initial activity but also to their stability. The resulting activities and stabilities are correlated to the nanoparticle shape and size evolution, elemental bulk distribution, and detailed surface characteristics using CO oxidation, aberration-corrected scanning transmission electron microscopy (STEM) in combination with energy-dispersive X-ray (EDX) analysis, and *in situ* electrochemical Fourier transform infrared (FTIR) spectroscopy. Together, we provide a consistent picture of the surface chemical modification and

conditions that lead to a cathode catalyst Pt mass activity exceeding that of commercial Pt by a factor of ~25.

■ EXPERIMENTAL SECTION

Chemicals and Materials. Platinum(II) acetylacetonate (Pt(acac)₂, Pt 48% min.), nickel(II) acetylacetonate (Ni(acac)₂, 95.0%), tungsten hexacarbonyl (W(CO)₆, 97.0%), oleic acid (OAc, 90%), methanol (anhydrous, 99.9%), *n*-hexane (99%), 1-octadecene (90%), and cetyltrimethylammonium bromide (CTAB) were obtained from Alfa Aesar. Oleylamine (OAm, 98.0%), nickel chloride hexahydrate (NiCl₂·6H₂O 99.5%), sodium oleate (≥82% fatty acids), and dichloromethane (DCM) were obtained from Sigma-Aldrich. Dibenzyl ether (98%) was obtained from Fluka. Ethanol (100%) was obtained from VWR Chemicals. All chemicals were used as received.

Synthesis of Pt–Ni/C Octahedral Nanoparticles. Pt(acac)₂ (0.407 mmol), Ni(acac)₂ (0.934 mmol), OAm (48 mL), and OAc (32 mL) were added into a 100 mL three-neck-flask under reflux. The reaction mixture was stirred for 5 min under N₂ atmosphere at 60 °C, followed by raising the temperature to 130 °C. At this temperature W(CO)₆ (1.591 mmol) was added rapidly, N₂ purging was stopped, and the reaction mixture was heated to 230 °C and then stirred for 50 min. The reaction mixture was then cooled down to room temperature, and toluene (20 mL) and ethanol (60 mL) were added to the reaction mixture. The supernatant was removed by centrifugation (7800 rpm for 15 min) and dispersed in toluene (20 mL). The dispersion was added to a dispersion of Vulcan XC 72R (160 mg) in toluene (20 mL). The mixture was sonicated with an ultrasonic horn for 30 min. Afterward, ethanol (10 mL) was added, and the catalyst was centrifuged (7800 rpm for 15 min), washed with ethanol (30 mL) three times, and freeze-dried for 12 h.

Annealing of Pt–Ni/C Octahedral Nanoparticles. The synthesized powder (PtNi_{raw}) was heated to 180 °C at a rate of 10 K min⁻¹ in a tube furnace in synthetic air atmosphere and left for 30 min. After the tube furnace was purged with N₂ for 30 min, the atmosphere was changed to hydrogen (4%/Ar), and the temperature was raised at a rate of 10 K min⁻¹ to 300 °C (PtNi₃₀₀) or to 500 °C (PtNi₅₀₀) and left for 1 h. Afterward, it was allowed to cool to room temperature in N₂ (see Figure 1a).

Synthesis of Pt/C Reference. Platinum nanoparticles were synthesized using a wet-chemical synthesis route based on previous work.²⁷ In detail, Pt(acac)₂ (0.6 mmol), 1,2-tetradecanediol (1.2 mmol), OAm (300 μL), OAc (300 μL) were dispersed in dibenzyl ether (50 mL). The mixture was stirred under N₂ atmosphere to remove excess of oxygen. The temperature was then raised to 80 °C and held for 5 min to ensure complete dissolution of the Pt precursor and the reducing agent. Afterward, the temperature was raised with a ramping of 1 °C/min to 165 °C and kept for 1 h. The mixture was cooled down to room temperature, and ethanol (30 mL) and DCM (5 mL) were added. Vulcan XC 72R (100 mg) was dispersed in toluene (50 mL), the dispersion of Pt nanoparticles was added, and the mixture was stirred overnight. The supernatant was removed by centrifugation (7800 rpm, 15 min) and washed with ethanol (40 mL) three times. The received catalyst was freeze-dried overnight.

Synthesis of Ni/C Reference. Face centered cubic Ni nanoparticles were synthesized using a modified version of the metal oleate route.²⁸ An amount of NiCl₂·6H₂O (10 mmol), sodium oleate (20 mmol), Milli-Q water (>18 MΩ·cm) (15 mL), methanol (20 mL), and *n*-hexane (35 mL) was mixed in a 250 mL round-bottom flask. The reaction mixture was heated to ~65 °C for 4 h under reflux. The colored upper organic phase containing the Ni-oleate complex was cooled down to room temperature and washed five times with Milli-Q water to remove excess of salt. The Ni-oleate complex (1.4 mmol) was placed in a 100 mL 3-neck flask. The hexane phase was evaporated off at 115 °C for 1 h in air. The dried Ni-oleate complex was redispersed in 1-octadecene (40 mL), oleic acid (0.23 mL, 0.7 mmol), and CTAB (1.4 mmol). The reaction mixture was heated under N₂-protected atmosphere to 160 °C and held for 20 min to evaporate the remaining water under stirring. The mixture was then heated to 300 °C with a ramping of 5 °C/min. After 50 min, the reaction was cooled to room

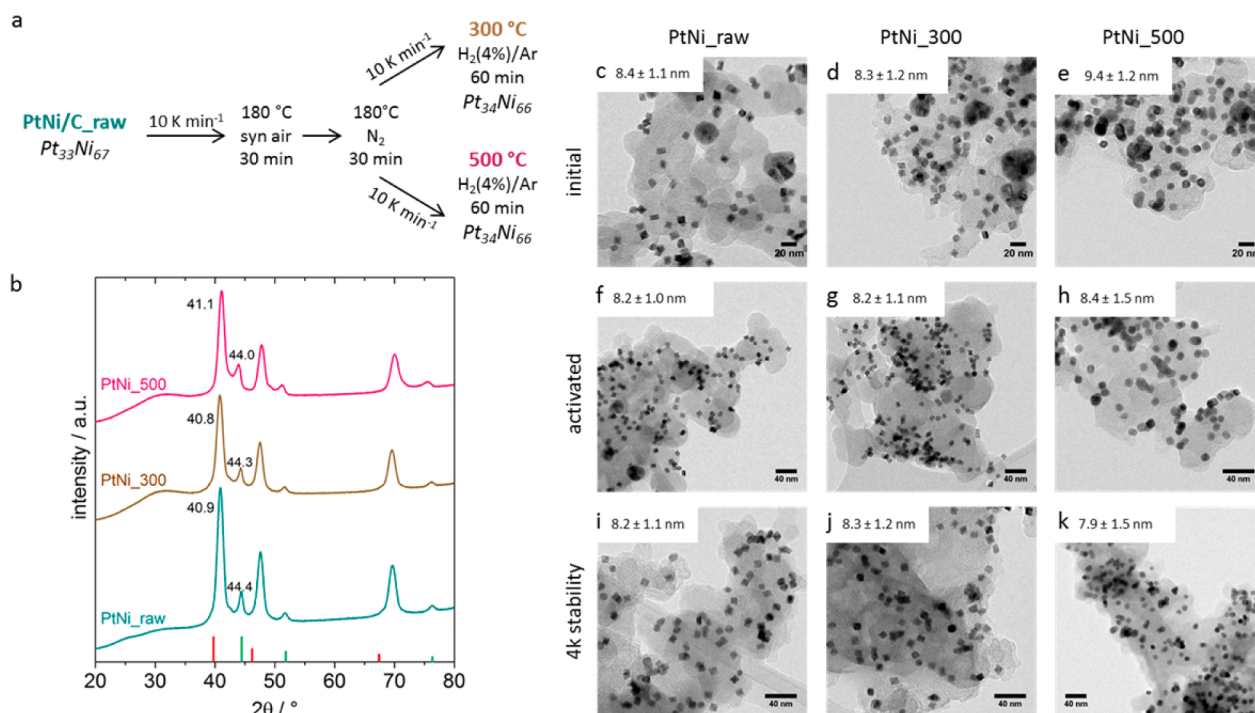


Figure 1. (a) Overview of samples, including the schematic process of the annealing procedure performed in a tube furnace. The compositions shown are determined by ICP OES physicochemical characterization of octahedral Pt–Ni/C. (b) XRD pattern of PtNi_raw, PtNi_300, and PtNi_500. Red columns correspond to pure Pt (PDF no. 00-004-0802) peaks and green columns to pure Ni (PDF no. 00-004-0850). On the right side are shown TEM images of the samples (c–e) in the initial state, (f–h) after activation, and (i–k) after 4k (4000 potential cycles) electrochemical stability treatment.

temperature using a water bath. The nanoparticles were subsequently supported on Vulcan XC-72R to a loading of 20 wt%. The carbon was dispersed in *n*-hexane (40 mL) and ethanol (20 mL) under sonication. The nanoparticles were added dropwise to the carbon under sonication during cooling with an ice bath. The nanoparticle–carbon mixture was left for additional 30 min in the sonication bath and for additional 20 h under magnetic stirring at room temperature. The supported nanoparticles were washed five times in hexane (15 mL) and ethanol (15 mL) by repetitive centrifugation at 7800 rpm for 10 min. The carbon-supported nanoparticles were finally freeze-dried and the powders stored under inert atmosphere until use.

Physico-chemical Characterization. (High-temperature, HT) XRD patterns were collected on a Bruker D8 Advance (Siemens KFL Cu 2K X-ray tube, and Lynx Eye detector) diffractometer in Bragg–Brentano geometry using a Cu $K\alpha 1$. The patterns were recorded between 20 and 80° with a step size of 0.05° and a 10 s measurement time at each step. High-temperature patterns were collected on a similar Bruker instrument with a Lynx Eye detector and Goebel mirror. The patterns were recorded between 35 and 55° with a step size of 0.06° and a measurement time of 8 s at each step. The samples were heated to 180 °C in synthetic air, followed by the heat treatment in 4% H₂/Ar. The heating and cooling rate was 10 K min⁻¹, and before every X-ray measurement the temperature was held for 15 min.

An inductively coupled plasma optical emission spectroscopy (ICP OES) analysis system (Varian) was used to determine the elemental composition of the synthesized particles. The selected wavelengths for the concentration determination were 203.646, 214.424, 224.552, 265.945, and 306.471 nm for Pt and 216.555, 221.648, 222.295, 222.486, 227.021, 230.299, and 231.604 nm for Ni.

Ex situ TEM was performed using a FEI Tecnai G2 20 S-TWIN with LaB₆ cathode, 200 kV accelerating voltage, and a resolution limit of 0.24 nm. Powder samples were dispersed on a 200 mesh Cu grid.

STEM was performed using a FEI Titan 80-200 (“ChemSTEM”) electron microscope with a C_s-probe corrector (CEOS GmbH) and a high-angle annular dark field (HAADF) detector.²⁹ The microscope was operated at 200 kV. In order to achieve “Z-Contrast” conditions, a

probe semi-angle of 25 mrad and an inner collection semi-angle of the detector of 88 mrad were used. Compositional maps were obtained with EDX using four large-solid-angle symmetrical Si drift detectors. For EDX elemental mapping, Pt L and Ni K peaks were used. The error of the EDX composition measurement was estimated to ± 2 at.%, and a minimum of 20 particles was investigated.

In situ heating TEM was performed using a Protochips Aduro heating holder in a FEI T12 Spirit TEM with a LaB₆ filament and 120 kV accelerating voltage. Sample powder was dispersed on a model E-AHA21 Protochips E-chip, which has an amorphous carbon film covering the viewing window.

To prepare an ink, 2.5 mg of catalyst was added to 2.5 mL of Milli-Q water, 7 μ L of Nafion (5 wt%), and 0.5 mL of isopropanol ($\geq 99.5\%$) and ultrasonicated for 15 min. An amount of 10 μ L of the ink was placed on a glassy carbon rotating disk electrode, which results in a Pt loading of 6–7 μ g cm⁻². The electrode was dried at 50 °C for 7 min to form a catalyst film.

For electrochemical characterization a conventional three electrode cell with a Pt gauze as counter electrode (Pt furled Pt 5 × 5 cm² mesh), a reference electrode (MMS = mercury–mercury sulfate, Hg/Hg₂SO₄ with potential $E = -0.723 V_{RHE}$, where RHE = reversible hydrogen electrode), and a glassy carbon working electrode (5 mm diameter) were used. The working electrode was always lowered into the electrolyte under potential control at 0.05 V_{RHE}. A 0.1 M HClO₄ electrolyte was used for electrochemical measurements (diluted from 70% concentrated HClO₄, 99.999% trace metal bases, Sigma-Aldrich with Milli-Q water). All measurements were controlled with BioLogics potentiostat SP-150 or SP-200 (Science Instruments).

The electrochemical activation was performed via potential cycling between 0.05 and 1.0 V_{RHE} with a scan rate of 100 mV s⁻¹ for 20 cycles under N₂ protected atmosphere.

To evaluate the H_{upd}-based electrochemically active surface area (ECSA), the last cycle which was recorded with 100 mV s⁻¹ before the activity measurements was selected. The cyclic voltammetry was carried out by cycling between 0.05 and 1.0 V_{RHE} with a scan rate of 100 mV s⁻¹ under N₂ atmosphere. The charge values (Q_H) were

calculated by integrating the respective cyclic voltammogram (CV) between 0.05 and 0.4 V. The measured Q_{H} values were normalized with respect to the theoretical value of $Q_{\text{H}}^{\text{theo}} = 210 \mu\text{C cm}^{-2}$, which is assuming a one-electron transfer between one H atom and one Pt atom.

For CO oxidation, the electrolyte was saturated with N_2 for 15 min. Afterward, the working electrode was lowered into the electrolyte under potential control at 0.05 V_{RHE} and with 400 rpm rotation speed. The gas was then switched to CO and the bubbling maintained for another 10 min followed by a gas change to N_2 again in order to remove CO from the electrolyte. Three CVs were recorded between 0.05 and 1.0 V with a scan rate of 50 mV s^{-1} and 0 rpm rotation. To determine the CO-based electrochemical active surface area, the voltammogram after the CO strip was subtracted from the CO-stripping voltammogram. The positive area of the resulting peak was integrated to obtain the CO charge value (Q_{CO}). The measured Q_{CO} value was normalized with respect to the theoretical value of $Q_{\text{CO}}^{\text{theo}} = 420 \mu\text{C cm}^{-2}$.

The catalytic activity of the catalysts was measured by linear sweep voltammetry. It was performed in oxygen saturated electrolyte (after at least 15 min of bubbling) in a potential range between 0.05 and 1.0 V_{RHE} with a scan rate of 5 mV s^{-1} and a rotation speed of 1600 rpm. The kinetic currents were calculated using eq 1, where j is the

$$\frac{1}{j} = \frac{1}{j_k} + \frac{1}{j_d} \quad (1)$$

measured current density at 0.9 V, j_d is determined in the diffusion-limited current area, and j_k is the calculated kinetic current density. All presented current densities are iR corrected, where the uncompensated ohmic resistance (R) was determined by potential electrochemical impedance spectroscopy (PEIS) at 0.4 V_{RHE} .

Stability measurements were performed via potential cycling between 0.5 and 1.0 V_{RHE} with a scan rate of 50 mV s^{-1} in N_2 saturated 0.1 M HClO_4 with 0 rpm. Before and after each stability protocol three CV cycles between 0.05 and 1.0 V_{RHE} at a scan rate of 100 mV s^{-1} were recorded.

Attenuated total reflection (ATR) FTIR spectroscopy was carried out in a modified ATR-FTIR setup which allows for the investigation of supported nanoparticle ink films almost identical with standard rotating disc electrode films.³⁰ The ink solution was prepared by adding 0.5 mL of Milli-Q water and 0.5 mL of isopropanol to 1.0 mg of catalyst powder followed by mixing with a probe-sonifier. The ink solution of supported electrocatalysts was deposited directly onto the ATR prism, avoiding intensity loss due to the lack of a sputtered layer of a conducting material such as Au. The electrochemical connection was made via a carbon cloth material that provides a reservoir of electrolyte over the catalyst, minimizing mass transport limitations and polarization effects. The spectra were collected in a custom-made glass cell with a Bruker Vertex 70v FTIR spectrometer equipped with a mercury-cadmium-telluride (MCT) detector cooled with liquid nitrogen. A platinum mesh was used as counter electrode and a RHE for reference fabricated by purging H_2 over a Pt-mesh. All *in situ* electrochemical measurements were controlled using a Metrohm Autolab PGSTAT204 potentiostat. An unpolarized beam was focused with a Pine Veemax II onto the sample spot of the cell. The spectral resolution was set to 4 cm^{-1} , and 100–107 interferograms were collected and averaged for each presented spectrum. Spectra are given in reflectivity units defined as $R/\Delta R = (RE_2 - RE_1)/RE_1$, with two single beam spectra R at applied potentials E_1 and E_2 . Here, the reference spectrum RE_1 was collected in the same electrolyte (0.1 M HClO_4) immediately before the investigated potential scan at the respective start potential. A ZnSe hemisphere was used as the IR window, and an ink of the electrocatalyst sample (1.0 mg in 0.5 mL of isopropanol and 0.5 mL of Milli-Q water) was deposited on the prism on the IR beam ATR focus spot and contacted with Toray Paper O30 carbon cloth and a Pine glassy carbon rod fixating the carbon cloth. The complete beam pathway was under vacuum more than 24 h prior to each measurement. The positions of the bands were determined by

taking the band maximum, or, for bipolar bands, by taking the mean value of the maximum and the minimum. Reported error bars are presenting the standard deviation between at least three different and independent measurements of freshly prepared catalyst films.

RESULTS

Synthesis. Shape-controlled Pt–Ni nanoparticles were synthesized using a wet-chemical approach including oleic acid and oleylamine as surfactants and solvents, after which the supported nanoparticles were exposed to different post-synthesis treatments: washing with ethanol after synthesis (PtNi_raw), washing and annealing at an upper temperature of 300 °C (PtNi_300), and washing and annealing at an upper temperature of 500 °C (PtNi_500) (Figure 1a). The particles were annealed at 180 °C in synthetic air in order to oxidize remaining organic surfactants from the synthesis and subsequently treated at elevated temperatures in reducing atmosphere for the purpose of ensuring a metallic surface. PtNi_raw should serve as an un-annealed reference and has experienced no thermal treatment. Details on that annealing procedure can be found in the Experimental Section and in Figure 1a. All three catalysts exhibit a composition between $\text{Pt}_{34}\text{Ni}_{66}$ and $\text{Pt}_{33}\text{Ni}_{67}$ and a Pt-based mass loading on Vulcan of around 15–16 wt%_{Pt}, measured by ICP OES. The compositions are presented in Figure 1a.

Ex Situ XRD Analysis. The XRD patterns (Figure 1b) of all three samples show peaks identifying a Pt-rich Pt–Ni alloy at 2θ values of around 41° (111), 47° (200), and 70° (220). Additional smaller peaks can be observed at around 44°, 52°, and 76° (Figure 1b) which indicate the presence of a Ni-rich phase. As suggested by EDX mappings discussed later on, these Ni-rich phases exhibit a small Pt-rich core, which might cause a separate Pt peak, which probably is superimposed by the alloy peak. Comparison of the peak positions of the Pt–Ni (111) peaks for all materials (numbers in XRD pattern Figure 1b) reveal a shift to slightly larger Bragg angles with increasing annealing temperature above 300 °C, while the Ni-rich (111) peaks shift in the opposite direction. To support this assumption Rietveld analysis was performed in order to obtain information about the different alloy phases. Generally, all patterns are described by two PtNi phases and one Ni phase, all based on Pt fcc. The phase compositions (Table S1), refinement patterns (Figure S1), and refinement details (Table S2) are shown in the Supporting Information (SI). According to these results, we achieve a main PtNi phase with a constant ratio (~65%) at all three temperatures. With increasing temperatures the concentration of the Ni phase decreases, whereas the second PtNi phase increases. The Ni phase of PtNi_500 exhibit a larger lattice constant in comparison to the other samples which indicates an interdiffusion of the big particles with the observed small Pt-rich cores as seen in STEM EDX; forming a new alloy phase within the big particles. With that we conclude, that the main changes during annealing are happening on the big Ni-rich particles, which possibly alloy with their small Pt cores upon annealing. The main PtNi phase (~65%), on the other hand, has a constant ratio during annealing up to 500 °C. But it has to be mentioned, that its lattice constant is slightly decreasing after annealing at 500 °C (Table S2). *In situ* TEM heating experiments discussed below provide further information for this suggestion.

Ex Situ TEM Analysis. TEM images of the three samples before electrochemical treatment (“initial”), are presented in

Figure 1c–e. PtNi_{raw} and PtNi₃₀₀ particles are mostly octahedrally shaped with a narrow size distribution (Figure S2a,b) and an average edge length of 8.4 ± 1.1 and 8.3 ± 1.2 nm, respectively. However, after 500 °C annealing, the previously octahedral particles became predominantly spherical in shape, with an average diameter of 9.4 ± 1.2 nm. In addition to the octahedral particles, large, roughly spherical particles are observed in the initial samples with a size around 20 nm in diameter. According to STEM EDX shown and discussed further below these particles mostly consist of Ni. By counting the number of octahedral and big particles on different catalyst agglomerates, the ratio of big Ni particles was estimated to be only ~4%. These Ni-rich particles offer great opportunity to study effects of temperature and electrochemical characteristics not only on octahedral-shaped nanoparticles but also on less precious components like Ni. For all three samples the nanoparticles are homogeneously distributed on the carbon support.

In Situ TEM Analysis during Annealing. In order to study the morphological changes of the samples during annealing, *in situ* heating TEM experiments were performed (Figure 2). During the experiment, the specimen was heated in

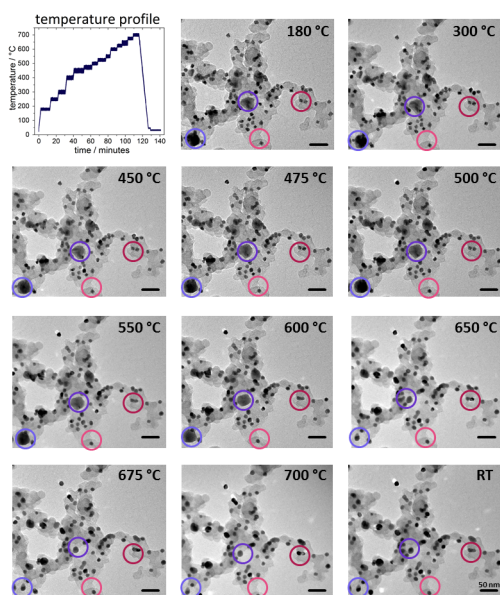


Figure 2. *In situ* heating TEM images of PtNi_{raw} in vacuum from room temperature (RT) up to 700 °C (temperature profile). Purple circles indicate the evolution of the bigger, Ni-rich particles during temperature treatment. Pink circles are emphasizing the change of the octahedral particle shape during heating. Numbers in the 180 °C image are referring to Figure S3.

vacuum with the temperature increasing incrementally from 180 to 700 °C during approximately 2 h. The octahedral particles maintain clear edges up to 450 °C, but at temperatures higher than 475 °C the corners start to round off, and at 525 °C some closely neighboring particles start to coalesce. Figure S3 shows enlarged images of the marked particles from Figure 2 to facilitate traceability of nanoparticle changes. This observation confirms the *ex situ* observation that the octahedral particles had become spherical in PtNi₅₀₀. Above 600 °C, the large Ni-rich particles appear to shrink rapidly, leaving behind a smaller particle that appears stable above 675 °C. This can most likely be explained by Ni atoms from the Ni-rich phase becoming

mobile at high temperature and incorporating into the Pt-rich particles. This is consistent with the *ex situ* XRD observations in Figure 1b which indicated a convergence of the different phase compositions with increasing temperature.

In Situ XRD Analysis during Annealing. To better understand our observations during the *in situ* heating TEM experiments, complementary *in situ* high temperature XRD (HT XRD) experiments were performed. In particular, the position of the (111) diffraction peak was monitored to follow our hypothesis about a gradual Ni incorporation into the prevalent Pt–Ni alloy phase. To ensure good comparability of the data, *in situ* XRD patterns were measured under identical conditions as *ex situ* data, where the cleaning step in synthetic air was followed by reduction in hydrogen/argon (see Figure 1). The temperatures were chosen in the same range to match the *in situ* TEM experiment (see temperature profile in Figure S4c). The obtained XRD patterns are depicted in Figure 3, where the pattern of the initial sample (PtNi_{raw}) measured at 30 °C in synthetic air is shown in turquoise. The main (111)-

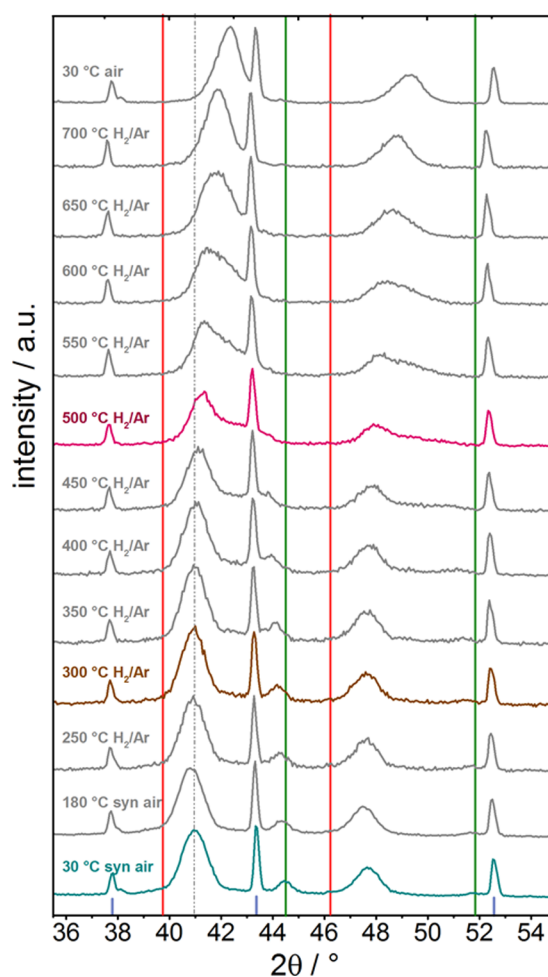


Figure 3. *In situ* heating X-ray diffractograms of the (111) and (200) signals of PtNi_{raw} in the temperature range between 30 and 700 °C. Gas atmospheres were chosen comparably to the *ex situ* annealing conditions in the tube furnace, and temperature range was chosen according to the *in situ* heating TEM experiment. Red lines are assigned to pure Pt peaks, green lines to pure Ni, and blue columns to Al₂O₃ caused by the high-temperature holder. The dashed line at around $2\theta = 43^\circ$ provides orientation of the shift of the main alloy peak.

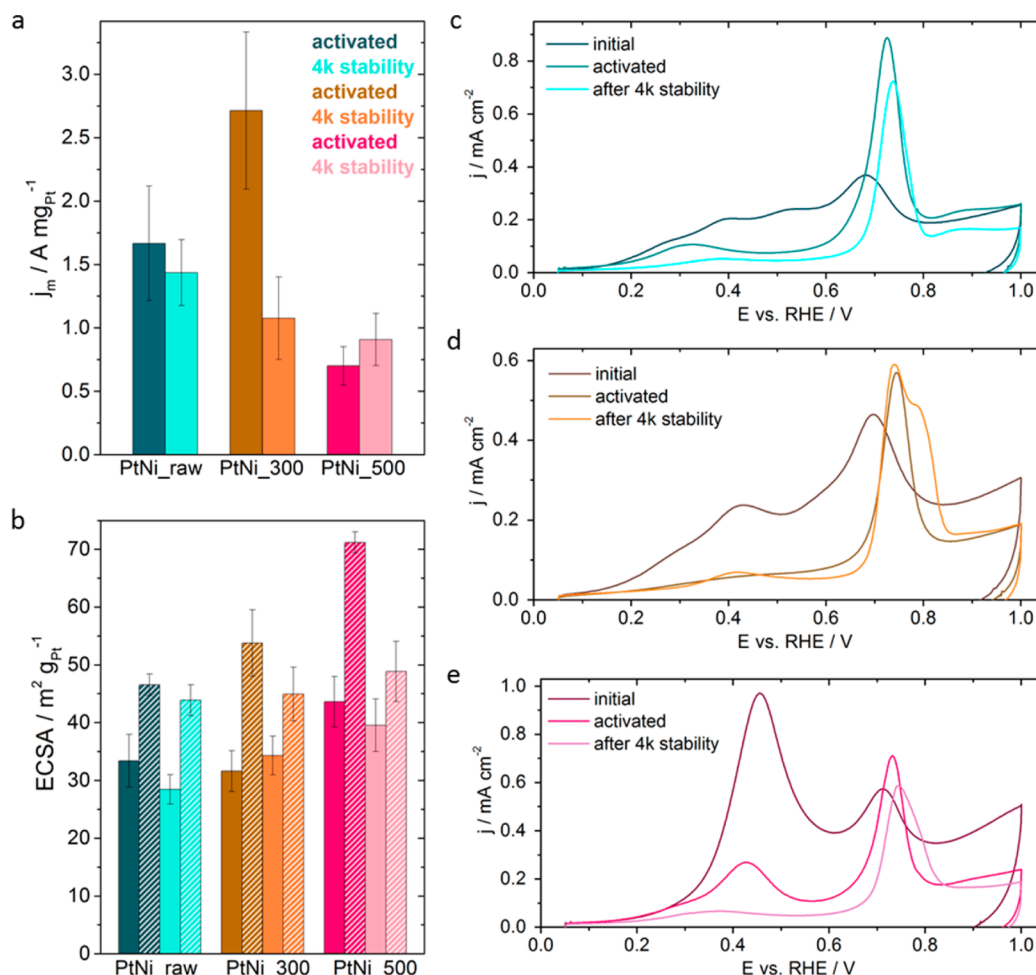


Figure 4. (a) Electrochemical ORR activity of the activated state (after 20 cyclic voltammograms (CV) activation) and after 4k stability test (4000 CV stability measurement) evaluated at 0.9 V; ORR was measured in O_2 sat. 0.1 M $HClO_4$ between 0.05 and 1.0 V_{RHE} with 5 mV s^{-1} , 1600 rpm, and were iR corrected. (b) Electrochemically active surface area determined by integration of the hydrogen under potential deposition region (H_{upd}) (solid colors) and the CO oxidation peak (striped colors) after activation and 4k stability test. The error bars depicting the standard deviation between at least three different and independent measurements of freshly prepared catalyst films. (c–e) Positive CO oxidation profile of the initial samples, activated and after 4k stability test. H_{upd} values were evaluated from CVs measured in N_2 sat. 0.1 M $HClO_4$ between 0.05 and 1.0 V_{RHE} with 100 mV s^{-1} . CO oxidation was performed in N_2 -saturated 0.1 M $HClO_4$ between 0.05 and 1.0 V_{RHE} with 50 mV s^{-1} and 0 rpm. 4k stability tests were measured in N_2 -saturated 0.1 M $HClO_4$ between 0.5 and 1.0 V_{RHE} with 50 mV s^{-1} .

alloy peak is tagged by the gray dotted line at $2\theta = 40.94^\circ$. With increasing temperature the maximum of the peak is shifting to higher 2θ values, showing a similar trend as observed for the *ex situ* patterns, and becomes slightly asymmetric. The Ni peak at $2\theta = 44.48^\circ$, however, was slightly shifting to lower values during heating. After the heat treatment and cooling down to 30°C , the (111) peak shifted to $2\theta = 42.38^\circ$, and the previously present Ni peak at $2\theta = 44.48^\circ$ is no longer visible. The discrepancy between the absolute values of the *ex situ* and *in situ* XRD patterns could be caused mainly by the temperatures and the gas atmospheres at which the patterns were recorded.

To correct for the influence of the temperature itself on the peak shifts and lattice constant changes, identical control HT XRD experiments were performed using carbon-supported pure Pt and pure Ni metal nanoparticles of comparable size. Figure S4a,b show the diffraction pattern of Pt/C and Ni/C and the impact of temperature on the position of the (111) peak. Figure S4d is summarizing the changes of the maximum peak position as a function of the temperature. For the pure Pt and Ni metal nanoparticles, the Bragg angles are decreasing

with increasing temperature due to an expansion of the metal lattice while the Bragg angles for the Pt–Ni alloy are showing the opposite trend. These findings confirm the assumption that Ni is incorporated in the main Pt–Ni alloy during annealing in hydrogen to form an alloy and therefore, the peak is shifting to higher 2θ values in contrary to the usual metal behavior. The slightly asymmetric shape of that peak suggests a non-uniform incorporation of Ni into Pt–Ni.

The combined results from the *in situ* and *ex situ* XRD and TEM experiments suggest that annealing in oxygen followed by hydrogen atmosphere leads to more Ni-rich alloys compared to the PtNi_raw particles which could be followed by the peak position in XRD. In more detail, two processes are taking place during annealing, as suggested and supported by the combination of Rietveld analysis, *in situ* heating TEM, and *in situ* XRD: (1) formation of a Ni-rich Pt–Ni alloy within the big Ni particles by alloying Pt from the core with surrounding Ni at temperature up to $\sim 500^\circ\text{C}$, and (2) incorporation of Ni-rich alloys into neighboring former octahedral particles at temperature above 600°C .

Cyclic Voltammetry. The particles were then subjected to cyclic voltammetry under oxygen-free conditions in a three-electrode rotating disc electrode setup and subsequently tested for the catalytic ORR. The oxygen-free cyclic voltammetric profiles of each catalyst are shown in Figure S5a–c. Evolution of characteristic waves inside the underpotential hydrogen deposition/desorption region ($0.05\text{--}0.4\text{ V}_{\text{RHE}}$) suggested the gradual faceting of the octahedral particles and, in correlation with the catalytic data, gave insight into the observed time evolution of the catalytic ORR behavior. Figures S5a–c display the “initial” state (the very first cycle), the “activated” state (the 20th cycle), and the state after 4000 potential cycles (“after 4k cycles”). The surface redox features that during the first cycles were quite comparable for PtNi_raw and PtNi_300 (Figure S5a,b), however, grew more pronounced during the 20th cycle. After the 4k stability test, PtNi_300 displayed a new distinct redox feature at $0.4\text{ V}_{\text{RHE}}$, possibly caused by the formation of an additional facet during the surface restructuring of the particles. The CVs of PtNi_500 generally deviated from the ones of PtNi_raw and PtNi_300. Only one pronounced redox peak is visible in the H_{upd} region, with the strongest intensity in the activated state. Correlating the electrode potentials of these redox features with literature allows for insight in the presence and accessibility of specific surface: The Pt surface–adsorbate adsorption energy of H_{ad} , and hence the electrochemical redox potential, is increasing in the order $(110) < (100) < (111)$,³¹ which affects the resulting ORR activity in distinctly different ways.

Catalytic ORR Activity and Stability. The mass-based electrocatalytic ORR activities are reported in Figure 4a, obtained by linear sweep voltammetry (LSV) after electrochemical activation by surface conditioning during 20 cycles (denoted as “activated” in Figure 4) and after stability testing consisting of 4000 electrochemical cycles (denoted as “4k stability”) (LSVs are shown in Figure S5d). After activation, the mass-based activity of PtNi_300 reached a *reproducible* high value of $2.7\text{ A mg}_{\text{Pt}}^{-1}$, by far outperforming the activity of PtNi_raw ($1.7\text{ A mg}_{\text{Pt}}^{-1}$) and PtNi_500 ($0.7\text{ A mg}_{\text{Pt}}^{-1}$). After the stability test, the activity of PtNi_300 dropped to $1.1\text{ A mg}_{\text{Pt}}^{-1}$, corresponding to a loss in activity of 60%. In contrast, the activities for PtNi_raw and PtNi_500 did not exhibit any statistically significant degradation.

TEM Morphology. In order to explain and understand the distinctly different time evolutions of the catalytic ORR activity and stability of the three catalysts, first, we considered the possible role of changes in octahedral particle morphology. TEM images were taken after each electrochemical treatment. Figure 1f–k presents representative TEM images of PtNi_raw, PtNi_300, and PtNi_500 after activation and after 4k stability measurement. The octahedral shape of PtNi_raw and PtNi_300 remained unchanged after the activation and after the 4k stability test. Thus, the morphology of the octahedral PtNi particles itself does not account for the observed changes in ORR activity. However, as expected for the acidic environment, the images evidence that large (Ni-rich) particles disappeared already after activation for PtNi_300 and after the 4k stability test for the PtNi_raw sample. TEM images of PtNi_500 after electrochemical treatment did not show any significant variations. Particles rarely coalesced after the 4k stability test (Figure 1i–k), and the particle size was stable within the error (Figure S2), so changes in activity cannot be a result of that.

CO Stripping. To learn more about the possible influence of the catalyst surface composition on the drastic activity/stability differences between the annealed and non-annealed octahedral Pt–Ni particles, electrochemical CO oxidation (“CO stripping”) according to the reaction equation



was used. Electrochemical CO stripping is known to be an extremely surface-sensitive characterization of the surface composition and defect density. Figure 4c–e presents the CO oxidation curves of the three catalysts at the various testing stages. The broad faradic features of the anodic CO voltammograms, considering their early CO oxidation onset, suggest that the initial particles (“initial”) are quite Ni-rich in and below their surfaces.³² Such Ni-rich domains are capable to activate water molecules and form Ni(oxy)hydroxides on their surface which reactively remove CO adsorbed on neighboring Pt sites as early as $0.2\text{ V}_{\text{RHE}}$. Ni dissolution and subsurface dealloying is likely contributing to these observed broad voltammetric profiles as well, especially prominent for the PtNi_raw catalyst with Ni dissolution appearing between 0.4 and $0.5\text{ V}_{\text{RHE}}$.³³ In the activated state, the broad features between 0.2 and $0.7\text{ V}_{\text{RHE}}$ are generally weakened. Noteworthy is the basically flat, only gradually increasing voltammetric profile of the most active PtNi_300 catalysts with its sharp CO oxidation wave between 0.7 and $0.8\text{ V}_{\text{RHE}}$. Here, Ni appears to be distributed evenly in subsurface regions suppressing any distinct redox wave around $0.4\text{ V}_{\text{RHE}}$. This is in contrast to the behavior of the other activated catalysts with their characteristic Ni domain-assisted CO oxidation waves around $0.4\text{ V}_{\text{RHE}}$ (see especially for the PtNi_500 catalyst) indicating Ni surface domains with activated oxygenates.^{12,18,25} The PtNi_300 continues to display an exceptional behavior, as after 4000 cycles a CO oxidation wave around $0.4\text{ V}_{\text{RHE}}$ is appearing, contrary to the other two catalysts whose features are continuously fading due to Ni electro-dissolution. Furthermore, an additional CO stripping current shoulder appears at a more anodic potential of $0.8\text{ V}_{\text{RHE}}$, which is also present for PtNi_500, but by far not that strongly pronounced.

According to literature, an early CO oxidation onset is caused by the competing adsorption of CO and OH species due to the reduced binding energy of Pt alloyed with Ni, so the CO blocking effect is diminished.^{32,34} It is also important to consider the presence of a separate Ni-rich phase in terms of interparticle oxidation for some of the materials (all initial – Figure 1c–e; activated PtNi_raw – Figure 1f). López-Cudero et al. discussed the effect on CO oxidation potentials of interparticle oxidation on Pt nanoparticles.³⁵ As Ni sites are adsorbing OH species in favor of CO, they might have a large effect on the CO oxidation potential. Taking PtNi_raw after 0 CV as an example, three oxidation features can be observed in the anodic CO oxidation scan. CO can only be adsorbed on Pt sites of the particle, while OH species can also be adsorbed on Ni sites. Taking the additional Ni sites into consideration several OH adsorption sites are plausible: separate big Ni particle, Ni or Pt sites on the octahedral facets, and Ni or Pt sites on the octahedral edges and corners.³⁶ Thus, the presence of the big Ni particle could have an influence on the CO oxidation peak position. Since the early CO oxidation peak is less pronounced after activation, the presence of a separate Ni phase seems to play an important role for the initial particle characteristics.

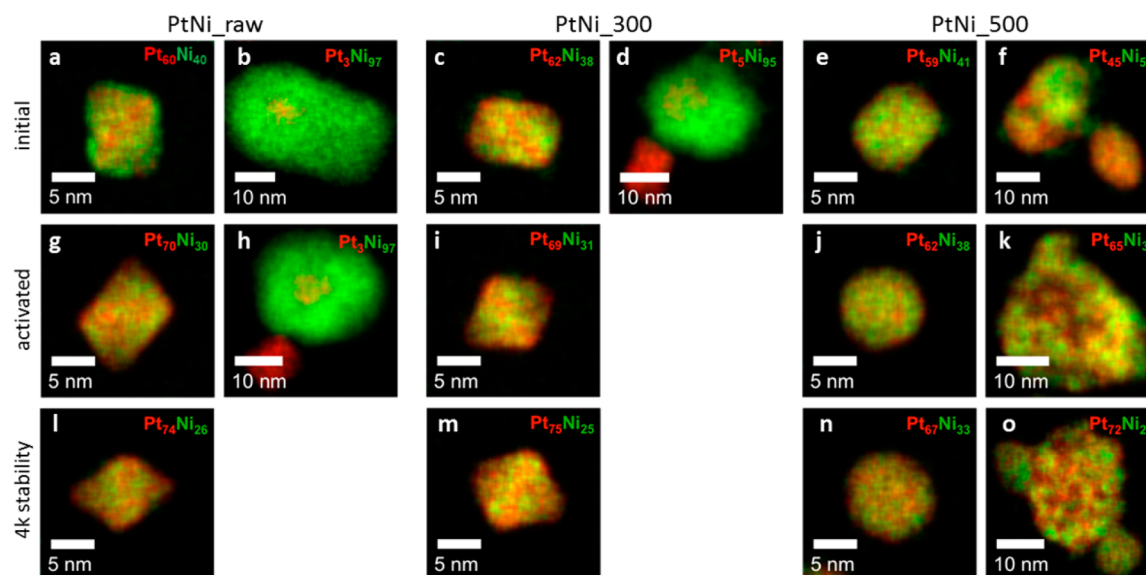


Figure 5. EDX elemental maps showing the composition of PtNi_raw (a,b,g,h,l), PtNi_300 (c,d,i,m), and PtNi_500 (e,f,j,k,n,o) in the initial conditions (a–f), after activation (g–k), and after 4k stability test (l–o). If present, also big irregular shaped mostly Ni-rich particles are depicted with their elemental distribution (b and h; d, f, and k; and o). A minimum of 20 particles were investigated for each sample in order to determine an average particle composition. Pt is shown in red and Ni in green.

The CO oxidation results indicate for PtNi_300 a stronger CO binding than both PtNi_raw and PtNi_500. PtNi_500, however, binds CO comparatively weakly, as most of it becomes oxidized at low potentials.

Electrochemical Surface Areas. From the discussed CVs and CO stripping voltammograms, the electrochemically active surface areas (ECSAs) were calculated. The values are reported in Figure 4b. The solid bars represent the ECSAs obtained by integrating the H_{upd} area, and the striped bars show the ECSA values obtained by integrating the CO oxidation area. For PtNi_raw and PtNi_500, the H_{upd} -based and the CO-based ECSAs are decreasing after the 4k stability test. For PtNi_300 this is only true for the CO-based ECSA, the H_{upd} -based ECSA is slightly increasing. The small differences are within the estimated error of the measurements. The CO-based ECSAs for Pt–Ni alloy systems typically are larger than the H_{upd} -based.^{32,34}

HAADF STEM and EDX Analysis. To further understand the differences in activity and stability, the atomic-scale elemental distribution of the particles was studied by STEM and EDX analysis. Figure S6 shows HAADF STEM images of Pt–Ni octahedral nanoparticles in different states and Figure 5 the corresponding EDX elemental maps.

The EDX map of the octahedral PtNi_raw nanoparticle, oriented close to a $\langle 110 \rangle$ zone axis, indicates an enrichment of Ni at the $\{111\}$ facets and a Pt-rich frame, which is pointed out by a Pt-rich stripe across the middle of the nanoparticles (Figure 5a). Additionally, a Ni-rich surface is visible. EDX quantification yields an average composition of Pt 60 at.% and Ni 40 at.% (shown particle Pt 59 at.%, Ni 41 at.%) of the particles in the initial state (Figure 5a). After activation, EDX quantification shows a decrease of Ni with an average composition of Pt 70 at.% and Ni 30 at.% (shown particle Pt 70 at.%, Ni 30 at.%). Furthermore, the EDX elemental map in Figure 5g shows a change in the distribution of Pt and Ni: Instead of a Ni-rich surface a thin Pt layer is observed at the outermost parts of the representative octahedron which can be interpreted as a thin Pt-rich skin on the facets of the octahedra.

As already shown by TEM (Figure 1i) the octahedral shape is retained after the 4k stability. The surface of the octahedron is still Pt-rich but the Pt layer appears a bit thicker in comparison to the state after activation. The average composition after the 4k stability test was Pt 74 at.% and Ni 26 at.% (shown particle Pt 74 at.%, Ni 26 at.%); hence, a slight change of the composition toward more Pt is observed after cycling in comparison to the state after activation.

In order to study the influence of annealing on the structural evolution during cycling, we investigated PtNi_300 octahedral nanoparticles which were treated at 300 °C in 4% hydrogen in the initial state, after activation, and after 4k stability test (Figure 5c,i,g and Figure S6c,i,m). While the EDX elemental map of the state after 300 °C as well as its activated state (Figure 5c,i) showed a comparable average Pt and Ni composition compared to the non-annealed PtNi_raw catalyst (Figure 5a,g) with Pt 62 at.%, Ni 38 at.% after 300 °C (shown particle Pt 65 at.%, Ni 35 at.%) and Pt 69 at.%, Ni 31 at.% after activation (shown particle Pt 68 at.%, Ni 32 at.%), the distribution of Pt and Ni is clearly changed comparing the PtNi_raw and PtNi_300 samples. While Ni is mostly distributed at the surface of the PtNi_raw octahedra, it is located more on the inside in the PtNi_300 octahedra. After activation, the elemental distribution was similar for PtNi_raw and PtNi_300, with a thin Pt-rich layer that remains in the annealed sample after 4k stability test compared to the thicker Pt layer observed in the non-annealed sample after the 4k stability test. Due to the low signal-to-noise ratio, the thickness is hard to determine. A rough estimation for the Pt-rich outer layer is 0.8 nm for PtNi_raw and 0.5 nm for PtNi_300 (see Figure S7). The average composition of the octahedral particles after 4k cycles was Pt 75 at.%, Ni 25 at.% (shown particle Pt 75 at.%, Ni 25 at.%), respectively. Hence, again a dissolution of Ni is observed during the potential cycling procedure.

In order to explain the comparable composition and elemental distribution of PtNi_raw and PtNi_300 after activation, even though the initial elemental distribution is different, it is reasonable to expect two different dissolution

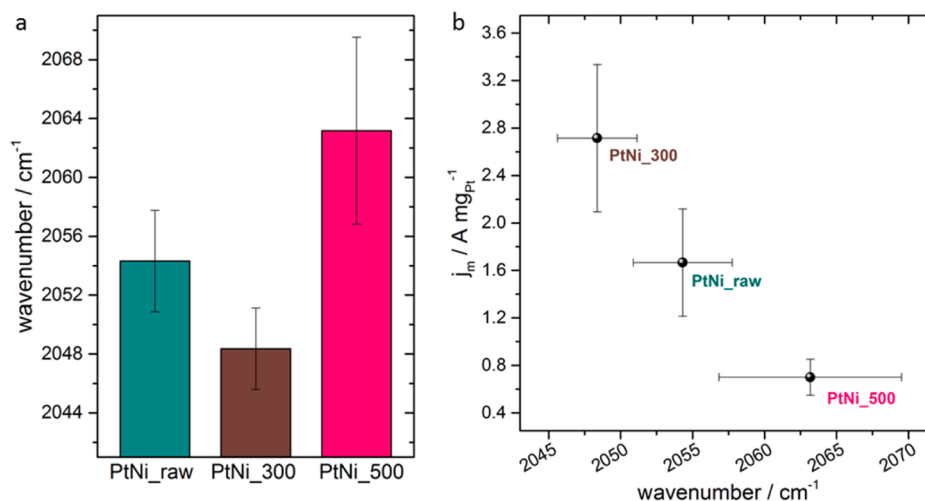


Figure 6. *In situ* FTIR spectroscopy measured in ATR mode. (a) Position of CO_{ad} band of the linear bounded CO collected at 50 mV_{RHE} in N₂ sat. 0.1 M HClO₄ for the different samples after electrochemical activation. (b) Correlation between ORR activity at 0.9 V_{RHE} and the CO_{ad} wavenumber obtained for the investigated set of particles. The error bars depicting the standard deviation between at least three different and independent measurements of freshly prepared catalyst films.

mechanisms: mainly Ni shell dissolution from the octahedral PtNi_{raw} nanoparticle surface (Figure 5a) resulting in the octahedron imaged in Figure 5g, losing around 10 at.% Ni, or dissolution from the Ni-rich PtNi₃₀₀ facets and Pt atom migration to the facets, losing around 7 at.% Ni. While that process is continued for PtNi₃₀₀ during additional 4k cycles, resulting in a Pt-shell, Ni dissolution from PtNi_{raw} is less pronounced, however resulting in a thicker Pt-shell. A comparable fast formation of a relatively thick Pt-shell, protecting the particle from further Ni-dissolution, could be a possible explanation.

Finally we investigated the PtNi₅₀₀ nanoparticles which were treated at 500 °C in 4% hydrogen, in the initial state, after activation, and after 4k stability (Figure 5 and Figure S6e,j,n). As also shown by TEM (Figure 1c) the octahedral shape turns into a more spherical shape after annealing at 500 °C. This shape transformation is accompanied by a change in the elemental distribution (Figure 5e) in comparison to the raw material and the particles after 300 °C annealing. The edges and corners become rounded off, and the compositionally segregated structure inside the particles is lost toward a more homogeneously alloyed structure of the PtNi₅₀₀ spherical particles (Figure 5e). After 500 °C annealing and activation (Figure 5j) as well as after the 4k stability test of PtNi₅₀₀, the Pt–Ni distribution remains unchanged (Figure 5n). Hence, the hydrogen treatment at 500 °C has a destabilizing effect on the octahedral shape as well as on the elemental distribution. The average composition of the Pt–Ni particles in the state after 500 °C, after activation, and after 4k stability is Pt 59 at.%, Ni 41 at.% (shown particle Pt 62 at.%, Ni 38 at.%), Pt 62 at.%, Ni 38 at.% (shown particle Pt 63 at.%, Ni 37 at.%), and Pt 67 at.%, Ni 33 at.% (shown particle Pt 67 at.%, Ni 33 at.%), respectively. Hence, Ni dissolution is observed as well, but comparatively more Ni is retained in the alloyed structure even after 4k stability test.

Beside the presence of octahedral nanoparticles in PtNi_{raw}, additional larger irregular-shaped nanoparticles are observed (Figure S6b). Therein, Pt-rich cores are encased by Ni shells (Figure 5b). The overall composition of these very large nanoparticles is Pt 3 at.% and Ni 97 at.%. These nanoparticles are also found after activation (Figure S6h) but not after the 4k

stability tests, which is due to the dissolution of their Ni shells after cycling in acidic media. The same is true for the 300 °C annealed sample (Figure S6d), but here the large nanoparticles are already dissolved after the activation treatment. In contrast, for the 500 °C annealed sample, the large nanoparticles are observed to exhibit a higher Pt (45 at.%) and a lower Ni content (55 at.%). The nanoparticle content changed to Pt 65 at.%, Ni 35 at.% after activation and Pt 72 at.%, Ni 28 at.% after 4k stability. Upon cycling, we observe a change of the structure as well as of the elemental distribution. After the 500 °C treatment, a more Pt-rich alloyed structure is observed (Figure S6f), which develops into a more sponge-like structure after activation and the 4k stability test (Figure S6k,o). This change is similar to the formation of porous structures already observed for big spherical Pt–Ni particles upon electrochemical dealloying.^{37,38}

In summary, our EDX elemental mapping results are in line with the XRD data and the CO stripping data. The origin of the dramatic activity difference between the activated PtNi_{raw} and PtNi₃₀₀ was not immediately obvious and will be clarified in the context of their stability.

***In Situ* Electrochemical FTIR Spectroscopy Studies.** To further probe the chemical nature of the catalyst particle surfaces and to correlate it with the distinctly different ORR activities, *in situ* electrochemical FTIR spectroscopy of surface-adsorbed CO was employed to monitor changes in the vibrational characteristics as a function of annealing at constant and varying electrode potentials (Figure 6 and Figure S8). The catalysts were compared in their activated state only. Figure 6a represents the wavenumbers of the stretching vibrations of linearly bonded CO, with PtNi₅₀₀ exhibiting the highest wavenumbers (2063 cm⁻¹), followed by PtNi_{raw} (2054 cm⁻¹), and then PtNi₃₀₀ (2048 cm⁻¹). All bands appear within the expected wavenumber range.³⁹ At this point it should be mentioned that the presence of Ni particles should not have a major impact on the observed stretching vibrations, as Ni is a weak CO binding surface and, if adsorbed, they should appear at lower wavenumber regimes.

In general, stronger CO surface chemisorption energies lower the C–O binding energy in the CO molecule and lower their C–O stretching frequency and wavenumber. Hence,

PtNi₃₀₀ exhibits a stronger CO chemisorption energy compared to PtNi_{raw} and PtNi₅₀₀.

Correlating these results with the corresponding ORR activities (Figure 6b) reveals that for shaped Pt–Ni alloys, stronger chemisorption induces higher catalytic ORR activities. We conclude that PtNi_{raw} and PtNi₅₀₀ bind surface species too weakly, resulting in overall lower ORR activities, while PtNi₃₀₀ exhibits a stronger, more optimal binding strength. Translating these finding into a volcano plot behavior, one would expect PtNi_{raw} and PtNi₅₀₀ on the weak-binding branch. PtNi₃₀₀ must be shifted in closer absolute proximity to the top of the volcano while PtNi₅₀₀ is farther away from the top on the weak binding branch. We need to mention that the observed wavenumber–ORR activity relation is likely to hold true for the family of shaped Pt–Ni particles with comparable size and may not apply to other chemically distinct types of Pt-based materials. Nevertheless, as pure Pt is binding CO stronger than Pt–Ni alloys, the experimental trend in stretching frequencies on Pt–Ni octahedra confirms a fairly Pt-rich surface for PtNi₃₀₀, followed by a Ni-rich surface for PtNi_{raw}, and the least Pt-rich surface for PtNi₅₀₀, which was exactly predicted by the *ex situ* CO stripping measurements (Figure 4c–e). This finding is important, as it may allow evaluation of ORR activity trends on the basis of their CO stripping profiles.

Figure S8d–f shows a representative set of *in situ* FTIR reflectivity spectra taken during CO stripping; Figure S8a–c shows the voltammetry. After the position of the linear CO stretching frequencies was investigated at a constant potential of 50 mV, the potential was slowly increased by 1 mV s⁻¹ to follow the CO oxidation *in situ* and to track the changes in CO stretching frequencies while increasing the potential. The corresponding *in situ* electrochemical faradaic stripping voltammetry (Figures S8a–c) was essentially, though not perfectly, consistent with the equivalent *ex situ* voltammetry shown in Figure 4c,d, which was conducted in a three-electrode RDE cell, not in the FTIR cell. This can be attributed to differences in FTIR cell geometry where the working electrode typically operates under diffusion limited conditions. Still, identical trends are found as in the *ex situ* CO stripping experiment. PtNi₅₀₀ exhibited a pronounced early CO oxidation peak, while it was less pronounced for PtNi_{raw}, and emerged at more anodic potentials for PtNi₃₀₀. The reflectivity FTIR spectra were reported every 95 mV and are referenced to the CO-free surface FTIR spectrum at 50 mV. All three materials are exhibiting the most intensive CO band at 50 mV, consistent with the chosen reference spectrum. With increasing potential all bands decline in intensity due to the oxidation of CO to CO₂. In comparison to PtNi_{raw} and PtNi₅₀₀, the highly active PtNi₃₀₀ catalyst exhibited a bipolar band, possibly indicating a slightly thicker catalyst film on the electrode. We refrain from plotting the evolution of the CO band position against the potential, as too many factors such as the CO coverage, particle size, catalyst film thickness, and the “Stark effect” may influence the position of the CO band during the application of an electrode potential. The various effects of adsorbed CO on Pt nanoparticles in combination with *in situ* FTIR experiments have been extensively described and discussed in detail in the past.^{40–44} However, effects on Pt–Ni alloy systems, especially octahedral shaped nanoparticles, are very poorly assessed to date. For that reason, we used the measured positions of the measured CO stretching frequencies only to make a relative comparison of the

binding and surface energies among the catalysts investigated in this study, to avoid comparison of the absolute band positions with values reported in literature.

To prove that PtNi_{raw} is a suitable un-annealed reference for all the used methods, the impact of only a 180 °C synthetic air and a 180 °C H₂/Ar annealing step according to Scheme S1 was investigated as shown in the Supporting Information. These two newly added samples should illustrate the minor impact of possible remaining surfactants on the particle surface. We performed a similar set of electrochemical and spectroscopic characterization methods in order to avoid any uncertainties as can be seen in Figures S9–S15.

DISCUSSION

On the Atomic Origin of the ORR Activity Differences.

Combining our findings from *ex situ* and *in situ* XRD, STEM-EDX, cyclic and scan voltammetry, *ex situ* RDE CO stripping, as well as *in situ* FTIR CO stripping/CO stretching frequencies, we are able to derive a more comprehensive molecular picture on the origin of the drastic variations in ORR activity and stability, which provides, in turn, a deeper understanding of the precise effect of annealing on the surface geometry and composition.

Moderate annealing at 300 °C followed by electrochemical activation by potential cycling resulted in an enhanced yet balanced chemisorption strength of adsorbed surface species compared to the un-annealed PtNi_{raw} and the 500 °C annealed PtNi₅₀₀ catalysts. *In situ* FTIR CO stretching frequencies, *ex situ* CO stripping, and EDX spectroscopy suggest the presence of a Pt enriched surface, even though no differences in the EDX elemental mappings could be observed for the activated PtNi₃₀₀ particles in comparison to PtNi_{raw}. This underscores the difficulties in unraveling the origin of electrocatalytic activity even using sophisticated STEM-EDX mapping due to a limited surface-compositional resolution. We show that CO adsorption is sensitive of extremely minute changes in the particle surface compositional structure, which even EDX spectroscopy is unable to resolve.

Although electrochemical activation of PtNi_{raw} and PtNi₃₀₀ leads to a similar elemental distribution as seen in the EDX mapping, the initial state of the particles appears to have an equally great influence on the resulting surface characteristics and hence on the ORR activities, as indicated by the *in situ* FTIR/CO adsorption study. It has to be mentioned, that remaining ligands from the synthesis on the particle surface should play a minor role in terms of activity and stability, which has been also shown by the comparison of different annealing treatments at 180 °C (see Figures S9–S15). The short-lived and evidently very active surface state after activation was no longer present after the 4k stability test of PtNi₃₀₀. This was because the stability-tested catalysts displayed a Pt-richer particle surface compared to its activated state, evidenced by the *ex situ* CO stripping profile and EDX mappings. Yet again, it was the CO stripping profiles that revealed subtle but highly important differences: The CO stripping profile of the PtNi₃₀₀ catalyst after the 4k stability test in Figure 4d displayed the presence of a new faradaic CO stripping wave at more anodic potentials attributable to a newly formed Pt–Ni phase with distinct atomic composition or surface structure. Closer inspection of the catalyst-based voltammograms in Figure S5 revealed that the PtNi₃₀₀ catalyst underwent more pronounced surface faceting after 4k cycling suggesting a stronger development of {110} and {100}

facets in combination with the emergence of a platinum shell (Figure S5, dashed lines at around 0.15 and 0.25 V_{RHE}). Surface faceting is an ordering process where structurally and compositionally defined terraces and steps/kinks are formed under prolonged potential cycling. Additional evidence is given by HAADF images in Figure S6m, showing octahedral edges cut along the [100] direction, providing new reaction sites. PtNi_raw, in contrast, while exhibiting a similar CO stripping profile after activation as PtNi_300, showed no additional redox wave after the 4k stability test. Indeed, the characteristics of its main CO stripping peak, associated with the Pt-rich surface domains, remained essentially unchanged after the 4k stability test, and so did its EDX elemental mapping. Such Pt- or Pt-rich domains in the surface appear to help protect the particle from Ni corrosion/depletion and subsequent losses in ORR activity, as observed for PtNi_raw. The thinner Pt-shell of the PtNi_300 catalysts, on the other hand, was affected more severely by the 4k stability cycles, presumably due to subsurface Ni. Ni atoms in subsurface regions dissolved from surface, which aided the partial surface faceting into Pt-rich terraces and steps, whereas PtNi_raw with its Pt-richer surface remained in a slightly more stable state.”

PtNi_500 showed a distinctly different behavior in terms of particle shape, CO stripping profile, elemental composition of individual particles, and ORR activity and stability behavior. The catalytic ORR activity of octahedral PtNi nanoparticles is known to depend on shape or elemental atomic distribution.^{12,21} For PtNi_500 both phenomena apply. After the thermal annealing, the octahedral shape was no longer well defined (Figure 5e), and consequently a smaller ratio of {111} facets were exposed. In addition, the anisotropic elemental distribution inside the particles was lost in favor of a more homogeneously alloyed structure. This is why PtNi_500 was less active as activated catalyst in comparison to PtNi_raw and PtNi_300. Furthermore, during the electrochemical 4k stability test the particles became Pt enriched in comparison to their initial state (Figure 5e,j,n), which would explain the gain in ORR activity. Additionally, the initially Ni-rich particles became also more Pt-rich, resulting in additional reaction sites (Figure 5f,k,o). Those Ni-rich particles are no longer present for PtNi_raw and PtNi_300, for which no significant changes in shape and anisotropy could be observed, either. The CO stripping profile after 4k cycles again displays a newly formed redox wave at higher anodic potentials, although less pronounced than for PtNi_300, suggesting the formation of more faceted reaction sites. A mixture of different facets is reasonable to assume, due to the shape of the spherical particles, resulting in lower intensities of each peak, respectively. Furthermore, the former Ni-rich particles exhibit a sponge like structure including more defects which could provide additional reaction sites (Figures S6f,k,o).^{45,46} As suggested by the *in situ* FTIR-CO stripping, PtNi_500 is binding reactive surface species too weakly to achieve ORR activities as high as for PtNi_raw and PtNi_300. Oxidized surface Ni does not bind CO strongly either. A Pt-poor surface is evidenced by the *ex situ* CO stripping results as for both the initial and activated states have very broad and early CO oxidation peaks.

Our analysis reveals that a successful tuning of the Pt–Ni octahedral particle surface toward high catalyst activity and stability requires a sensitive balance between Ni enrichment in the surface and subsurface, shape stability, and fine structure of the particle surface, which is hard to achieve by synthetic wet-

chemical synthetic methods alone. Annealing in defined gas atmospheres, however, is a powerful and sensitive-enough tool to achieve such a careful fine-tuning of alloy nanoparticle surfaces to ensure optimal ORR activity.

CONCLUSION

We have shown that annealing of Pt–Ni-based shaped particles is an effective post-synthesis treatment to clean and modify particle surfaces in order to obtain high ORR activities and improved stabilities. We studied different parameters to gain a deeper understanding of the material during heat treatment. Therefore, *in situ* heating transmission electron microscopy and X-ray diffraction experiments were performed to follow the morphological and structural changes. We have proven that annealing at elevated temperatures in reducing atmosphere has an impact on the alloy composition as well as on the particle shape. Especially, if one would desire to preserve a certain particle shape, a temperature treatment must be carried out very carefully. As presented, an annealing protocol also has an influence on the electrocatalytic ORR activity and stability. While it is possible to boost the initial activity, compromises in terms of stability have to be made. By using a combination of electrochemical surface characterization techniques like CO oxidation and EDX spectroscopy, we were able to explain the observed activity and stability trends. Further and deeper understanding of the catalyst surface was received by *in situ* FTIR spectroscopy using CO as a probe molecule, showing a correlation between CO binding energies and ORR activity. Taking all used methods into consideration, it became evident that annealing could be used to efficiently and carefully tailor the catalyst surface, where inducing small changes in the surface–reactant binding energies could drastically help to improve the catalytic ORR activities. Furthermore, we conclude that a compromise between a very active and stable surface is required.

ASSOCIATED CONTENT

Supporting Information

The Supporting Information is available free of charge on the ACS Publications website at DOI: 10.1021/jacs.7b06846.

Particle size distribution histograms, *in situ* heating X-ray diffraction patterns of Pt/C and Ni/C, cyclic voltammograms, linear sweep voltammograms, HAADF STEM images, and FTIR reflectivity spectra with corresponding electrochemistry data, including Tables S1 and S2, Scheme S1, and Figures S1–S15 (PDF)

AUTHOR INFORMATION

Corresponding Author

*pstrasser@tu-berlin.de

ORCID

Elliot Padgett: 0000-0001-9034-2335

Peter Strasser: 0000-0002-3884-436X

Notes

The authors declare no competing financial interest.

ACKNOWLEDGMENTS

We thank the Zentraleinrichtung für Elektronenmikroskopie (ZELMI) of the Technical University Berlin for its support with TEM measurements and C. Spöri for his great help with the HT XRD experiments. Financial support was given by

Deutsche Forschungsgemeinschaft (DFG) grants STR 596/S-1 (“Shaped Pt bimetallics”) and HE 7192/1-1, and by the German Federal Ministry of Education and Research (Bundesministerium für Bildung und Forschung, BMBF) under grant 03SF0527A (“LoPlaKats”). E.P. acknowledges support from a NSF Graduate Research Fellowship (DGE-1650441). This work made use of Cornell Center for Materials Research Shared Facilities which are supported through the NSF MRSEC program (DMR-1120296).

REFERENCES

- (1) Vanysek, P. In *CRC Handbook of Chemistry and Physics*, 81st ed.; Lide, D. R., Ed.; CRC Press LLC: Boca Raton, FL, 2000.
- (2) Rudi, S.; Tuae, X.; Strasser, P. *Electrocatalysis* **2012**, *3* (3–4), 265–273.
- (3) Gan, L.; Cui, C.; Rudi, S.; Strasser, P. *Top. Catal.* **2014**, *57* (1–4), 236–244.
- (4) Oezaslan, M.; Hasche, F.; Strasser, P. *J. Electrochem. Soc.* **2012**, *159* (4), B444–B454.
- (5) Oezaslan, M.; Strasser, P. *J. Power Sources* **2011**, *196* (12), 5240–5249.
- (6) Asset, T. C.; Chattot, R.; Nelayah, J.; Job, N.; Dubau, L.; Maillard, F. *ChemElectroChem* **2016**, *3* (10), 1591–1600.
- (7) Kongkanand, A.; Subramanian, N. P.; Yu, Y.; Liu, Z.; Igarashi, H.; Muller, D. A. *ACS Catal.* **2016**, *6* (3), 1578–1583.
- (8) Wang, C.; Chi, M.; Wang, G.; van der Vliet, D.; Li, D.; More, K.; Wang, H.-H.; Schlueter, J. A.; Markovic, N. M.; Stamenkovic, V. R. *Adv. Funct. Mater.* **2011**, *21* (1), 147–152.
- (9) Paulus, U. A.; Wokaun, A.; Scherer, G. G.; Schmidt, T. J.; Stamenkovic, V.; Radmilovic, V.; Markovic, N. M.; Ross, P. N. *J. Phys. Chem. B* **2002**, *106* (16), 4181–4191.
- (10) Stamenkovic, V. R.; Fowler, B.; Mun, B. S.; Wang, G. F.; Ross, P. N.; Lucas, C. A.; Markovic, N. M. *Science* **2007**, *315* (5811), 493–497.
- (11) Strasser, P. *Science* **2015**, *349* (6246), 379–380.
- (12) Cui, C.; Gan, L.; Heggen, M.; Rudi, S.; Strasser, P. *Nat. Mater.* **2013**, *12* (8), 765–771.
- (13) Choi, S.-I.; Xie, S.; Shao, M.; Odell, J. H.; Lu, N.; Peng, H.-C.; Protsailo, L.; Guerrero, S.; Park, J.; Xia, X.; Wang, J.; Kim, M. J.; Xia, Y. *Nano Lett.* **2013**, *13* (7), 3420–3425.
- (14) Chen, C.; Kang, Y. J.; Huo, Z. Y.; Zhu, Z. W.; Huang, W. Y.; Xin, H. L. L.; Snyder, J. D.; Li, D. G.; Herron, J. A.; Mavrikakis, M.; Chi, M. F.; More, K. L.; Li, Y. D.; Markovic, N. M.; Somorjai, G. A.; Yang, P. D.; Stamenkovic, V. R. *Science* **2014**, *343* (6177), 1339–1343.
- (15) Huang, X.; Zhao, Z.; Cao, L.; Chen, Y.; Zhu, E.; Lin, Z.; Li, M.; Yan, A.; Zettl, A.; Wang, Y. M.; Duan, X.; Mueller, T.; Huang, Y. *Science* **2015**, *348* (6240), 1230–1234.
- (16) Li, M.; Zhao, Z.; Cheng, T.; Fortunelli, A.; Chen, C.-Y.; Yu, R.; Zhang, Q.; Gu, L.; Merinov, B. V.; Lin, Z.; Zhu, E.; Yu, T.; Jia, Q.; Guo, J.; Zhang, L.; Goddard, W. A.; Huang, Y.; Duan, X. *Science* **2016**, *354* (6318), 1414–1419.
- (17) Zhang, J.; Yang, H.; Fang, J.; Zou, S. *Nano Lett.* **2010**, *10*, 638.
- (18) Cui, C.; Gan, L.; Li, H.-H.; Yu, S.-H.; Heggen, M.; Strasser, P. *Nano Lett.* **2012**, *12* (11), 5885–5889.
- (19) Carpenter, M. K.; Moylan, T. E.; Kukreja, R. S.; Atwan, M. H.; Tessema, M. M. *J. Am. Chem. Soc.* **2012**, *134* (20), 8535–8542.
- (20) Choi, S.-I.; Xie, S.; Shao, M.; Lu, N.; Guerrero, S.; Odell, J. H.; Park, J.; Wang, J.; Kim, M. J.; Xia, Y. *ChemSusChem* **2014**, *7* (5), 1476–1483.
- (21) Beermann, V.; Gocyla, M.; Willinger, E.; Rudi, S.; Heggen, M.; Dunin-Borkowski, R. E.; Willinger, M.-G.; Strasser, P. *Nano Lett.* **2016**, *16* (3), 1719–1725.
- (22) Arán-Ais, R. M.; Vidal-Iglesias, F. J.; Solla-Gullón, J.; Herrero, E.; Feliu, J. M. *Electroanalysis* **2015**, *27* (4), 945–956.
- (23) Arán-Ais, R. M.; Solla-Gullón, J.; Gocyla, M.; Heggen, M.; Dunin-Borkowski, R. E.; Strasser, P.; Herrero, E.; Feliu, J. M. *Nano Energy* **2016**, *27*, 390–401.
- (24) Ahmadi, M.; Cui, C.; Mistry, H.; Strasser, P.; Roldan Cuenya, B. *ACS Nano* **2015**, *9* (11), 10686–10694.
- (25) Cui, C.; Ahmadi, M.; Behafarid, F.; Gan, L.; Neumann, M.; Heggen, M.; Cuenya, B. R.; Strasser, P. *Faraday Discuss.* **2013**, *162* (0), 91–112.
- (26) Gan, L.; Heggen, M.; Cui, C.; Strasser, P. *ACS Catal.* **2016**, *6* (2), 692–695.
- (27) Rudi, S.; Gan, L.; Cui, C.; Gliech, M.; Strasser, P. *J. Electrochem. Soc.* **2015**, *162* (4), F403–F409.
- (28) Park, J.; An, K.; Hwang, Y.; Park, J.-G.; Noh, H.-J.; Kim, J.-Y.; Park, J.-H.; Hwang, N.-M.; Hyeon, T. *Nat. Mater.* **2004**, *3* (12), 891–895.
- (29) Kovács, A.; Schierholz, R.; Tillmann, K. J. *Large-Scale Res. Facilities JLSRF* **2016**, *2* (A43), 1–4.
- (30) Erini, N.; Beermann, V.; Gocyla, M.; Gliech, M.; Heggen, M.; Dunin-Borkowski, R. E.; Strasser, P. *Angew. Chem., Int. Ed.* **2017**, *56* (23), 6533–6538.
- (31) Grozovski, V.; Solla-Gullón, J.; Climent, V.; Herrero, E.; Feliu, J. M. *J. Phys. Chem. C* **2010**, *114* (32), 13802–13812.
- (32) Rudi, S.; Cui, C.; Gan, L.; Strasser, P. *Electrocatalysis* **2014**, *5* (4), 408–418.
- (33) Strasser, P.; Koh, S.; Greeley, J. *Phys. Chem. Chem. Phys.* **2008**, *10* (25), 3670–3683.
- (34) van der Vliet, D. F.; Wang, C.; Li, D.; Paulikas, A. P.; Greeley, J.; Rankin, R. B.; Strmcnik, D.; Tripkovic, D.; Markovic, N. M.; Stamenkovic, V. R. *Angew. Chem., Int. Ed.* **2012**, *51* (13), 3139.
- (35) Lopez-Cudero, A.; Solla-Gullón, J.; Herrero, E.; Aldaz, A.; Feliu, J. M. *J. Electroanal. Chem.* **2010**, *644* (2), 117–126.
- (36) Clavilier, J.; Actii, K. E.; Petit, M.; Rodes, A.; Zamakhchari, M. A. *J. Electroanal. Chem. Interfacial Electrochem.* **1990**, *295* (1–2), 333–356.
- (37) Gan, L.; Cui, C.; Rudi, S.; Strasser, P. *Top. Catal.* **2014**, *57* (1–4), 236–244.
- (38) Gan, L.; Heggen, M.; O’Malley, R.; Theobald, B.; Strasser, P. *Nano Lett.* **2013**, *13* (3), 1131–8.
- (39) Li, L.; Zhou, L.; Ould-Chikh, S.; Anjum, D. H.; Kanoun, M. B.; Scaranto, J.; Hedhili, M. N.; Khalid, S.; Laveille, P. V.; D’Souza, L.; Clo, A.; Basset, J.-M. *ChemCatChem* **2015**, *7* (5), 819–829.
- (40) Pecharromán, C.; Cuesta, A.; Gutiérrez, C. *J. Electroanal. Chem.* **2002**, *529* (2), 145–154.
- (41) Maillard, F.; Savinova, E. R.; Simonov, P. A.; Zaikovskii, V. I.; Stimming, U. *J. Phys. Chem. B* **2004**, *108* (46), 17893–17904.
- (42) Park, S.; Tong, Wieckowski, A.; Weaver, M. J. *Langmuir* **2002**, *18* (8), 3233–3240.
- (43) Cuesta, A.; Couto, A.; Rincón, A.; Pérez, M. C.; López-Cudero, A.; Gutiérrez, C. *J. Electroanal. Chem.* **2006**, *586* (2), 184–195.
- (44) López-Cudero, A.; Cuesta, Á.; Gutiérrez, C. *J. Electroanal. Chem.* **2006**, *586* (2), 204–216.
- (45) Dubau, L.; Nelayah, J.; Moldovan, S.; Ersen, O.; Bordet, P.; Drnec, J.; Asset, T.; Chattot, R.; Maillard, F. *ACS Catal.* **2016**, *6* (7), 4673–4684.
- (46) Chattot, R.; Asset, T.; Bordet, P.; Drnec, J.; Dubau, L.; Maillard, F. *ACS Catal.* **2017**, *7* (1), 398–408.